



King Saud University

Arabian Journal of Chemistry

www.ksu.edu.sa  
www.sciencedirect.com



ORIGINAL ARTICLE

# Biosynthesis effect of *Moringa oleifera* leaf extract on structural and magnetic properties of Zn doped Ca-Mg nano-spinel ferrites



M.A. Almessiere <sup>a,b,\*</sup>, Y. Slimani <sup>b,\*</sup>, I.A. Auwal <sup>c</sup>, S.E. Shirsath <sup>d</sup>, M.A. Gondal <sup>e,f</sup>, M. Sertkol <sup>g</sup>, A. Baykal <sup>h</sup>

<sup>a</sup> Department of Physics, College of Science, Imam Abdulrahman Bin Faisal University, P.O. Box 1982, Dammam 31441, Saudi Arabia

<sup>b</sup> Department of Biophysics, Institute for Research and Medical Consultations (IRMC), Imam Abdulrahman Bin Faisal University, P.O. Box 1982, Dammam 31441, Saudi Arabia

<sup>c</sup> Department of Chemistry, Sule Lamido University, Kafin Hausa 731, Nigeria

<sup>d</sup> School of Materials Science and Engineering, University of NewSouth Wales, Kensington, Sydney, NSW 2052, Australia

<sup>e</sup> Laser Research Group, Physics Department & IRC-Hydrogen and Energy Storage, King Fahd University of Petroleum and Minerals Dhahran 31261 Saudi Arabia

<sup>f</sup> K.A.CARE Energy, Research and Innovation Center, King Fahd University of Petroleum & Minerals, Dhahran, 31261, Saudi Arabia

<sup>g</sup> Deanship of Preparatory Year, Imam Abdulrahman Bin Faisal University, P.O. Box 1982, Dammam 31441, Saudi Arabia

<sup>h</sup> Department of Nanomedicine Research, Institute for Research and Medical Consultations (IRMC), Imam Abdulrahman Bin Faisal University, P.O. Box 1982, Dammam 31441, Saudi Arabia

Received 29 April 2021; accepted 9 June 2021

Available online 18 June 2021

## KEYWORDS

Magnetic nanoparticles;  
*Moringa oleifera*;  
Green synthesis;  
Ultrasonic irradiation;  
Magnetic properties

**Abstract**  $Zn_xCa_{0.5-x/2}Mg_{0.5-x/2}Fe_2O_4$  ( $x = 0.0\text{--}0.6$ ) nano-spinel ferrite (NSFs) were prepared by ultrasonic irradiation with *Moringa oleifera* leaf extract (group A) and without *Moringa oleifera* leaf extract (group B). The synthesis done with *Moringa oleifera* leaf extract is green synthesis. The structure and morphologies of both group A and B NSFs were investigated by XRD, SEM, TEM, and FT-IR in details. The crystallite sizes of group A and B products were calculated as within the range of 11–17 nm and 16–28 nm, respectively. The magnetic features of different nanoparticles of group A and B NSFs have been investigated at room ( $T = 300$  K) and low ( $T = 10$  K) temperatures by means of a vibrating sample magnetometer (VSM). All samples

\* Corresponding authors.

E-mail addresses: [malmessiere@iau.edu.sa](mailto:malmessiere@iau.edu.sa) (M.A. Almessiere), [yaslimani@iau.edu.sa](mailto:yaslimani@iau.edu.sa) (Y. Slimani), [\(M.A. Gondal\)](mailto:magondal@kfupm.edu.sa).

Peer review under responsibility of King Saud University.



Production and hosting by Elsevier

displayed superparamagnetic (SPM) behavior at room temperature, with no or negligible coercivity and retentivity. Nevertheless, the different samples revealed opened M–H hysteresis loops at a temperature of 10 K, which indicates their ferromagnetic (FM) behavior at very low temperatures. The various magnetic parameters including the saturation magnetization ( $M_s$ ), remanent magnetization ( $M_r$ ), squareness ratio ( $M_r/M_s$ ), magneton number ( $n_B$ ), coercive field ( $H_c$ ), etc. were extracted. The  $Zn_xCa_{0.5-x/2}Mg_{0.5-x/2}Fe_2O_4$  ( $x = 0.0 – 0.6$ ) NSFs prepared using *Moringa oleifera* extract (Group A samples) displayed lower  $M_s$  values in comparison to NSFs prepared without using *Moringa oleifera* extract (Group B samples). Whereas, the coercivity is found to be larger in Group B samples than in Group A samples. These are mainly ascribed to the variations in particles size upon the use of *Moringa oleifera* extract. Compared to non-substituted  $Ca_{0.5}Mg_{0.5}Fe_2O_4$  NSFs, it is noticed that the  $M_s$  value increases with  $Zn^{2+}$  ions substitution. The increase of  $M_s$  value is ascribed to the strengthening of exchange interactions and redistribution of cations (particularly  $Fe^{3+}$  ions) within the spinel lattice. At  $T = 10$  K, the  $H_c$  value decreases with the rise of the  $Zn^{2+}$  content, which is attributed to the larger crystallites/particles that lead to the lower volume fraction of grains boundaries, which in turn conduct to less pinning of domain walls. The SQR values at 10 K for all NSFs of group A and B are between 0.2 and 0.3, which is below the theoretical limit of 0.5, reflecting the NPs consist of multi-magnetic domains. The obtained magnetic properties of group A NSFs are interesting, suggesting that this method could be considered as an alternative and effective green synthesis route with appropriate control of size, morphology, and physical features of magnetic nanoparticles.

© 2021 The Author(s). Published by Elsevier B.V. on behalf of King Saud University. This is an open access article under the CC BY license (<http://creativecommons.org/licenses/by/4.0/>).

## 1. Introduction

Nanoparticles are a submicron-sized matter of dimension 1–100 nm. On account of their high surface area to volume ratio, they exhibit novel properties compared to their bulk counterpart and hence formed the basis of nanotechnology (Vergaro et al., 2011; Aisida et al., 2020). In particular, magnetic nanoparticles exhibit superparamagnetism and the ability to become excited and produce heat when induced by a high-frequency magnetic field. However, the high surface area to volume ratio tends to promote surface disorder effects, which results in a lower magnetic moment compared to the bulk magnets (Alves et al., 2006; Yao et al., 2007). In this regard, the synthesis of nanoscale while retaining the magnetic character as found in bulk will be increasingly important. Typically, magnetic nanoparticles display size-dependent magnetic behaviors which are exploited in diverse applications such as catalysis, drug delivery, hyperthermia, sensing, water purification, data storage, microwave absorption, etc. (Amiri et al., 2019; Pastucha et al., 2019; Mapossa et al., 2020; Wang et al., 2017; Bektar et al., 2020). The nano-spinel ferrites (NSP) are complex oxides of the chemical formula  $MFe_2O_4$ . NSP belongs to the face-centered cubic crystal structure of space group  $Fd\bar{3}m$  (Asiri et al., 2018; Chavarriaga et al., 2020). The optical, magnetic, and electrical property of NSP solids is directly linked to the distribution of metal ions in the crystallographic sites of the crystal, this crystallographic site occupancy takes place at the atomic level during the synthesis process. The rational control of the physicochemical properties of the material for specific application is desired but remains a tricky task.

A pure bulk zinc ferrites  $ZnFe_2O_4$  is classified as normal spinel ferrites where  $Zn^{2+}$  and  $Fe^{3+}$  occupation the (A) and (B) sites respectively in the crystal lattice. Due to antiferromagnetic and superparamagnetic behavior.  $ZnFe_2O_4$  found a variety of advanced applications (Won et al., 2014; Liang et al.,

2020; dos Santos et al., 2019). In particular, the excessive application of lithium batteries in electric vehicles and electric grids compelled the design of batteries with unconventional electrodes that have a longer life cycle with enough power density, high energy at a low price. Interestingly  $ZnFe_2O_4$  has a large value of theoretical specific capacity of 1000.5 mAh/g, which is 7.44% higher than that of  $Fe_3O_4$  (Jiang et al., 2016). Thus, become a winning anode material for higher energy density applications (Xing et al., 2012; Zhang et al., 2020; Martinez-Julian et al., 2014; Zhou et al., 2015).

The parameters that affect the crystallinity, morphology, and magnetism of zinc ferrites can be the source of initial reactants and composition, pH, thermal treatments, and synthetic techniques. So far, several methods for the synthesis of Zn ferrite have been reported such as solid-state (Li et al., 2007), spray drying (Won et al., 2014), hydrothermal (Xing et al., 2012), ball milling (Fella et al., 2013), thermal decomposition (Srivastava et al., 2018), and electrochemical growth (Rivero et al., 2016). Metal substitutions also play a crucial role in physicochemical properties. Hussain et al. reported the CoGd substituted  $ZnFe_2O_4$  via co-precipitation approach (Hussain et al., 2018). The addition of CoGd increases both saturation magnetization and coercivity while decreases the grain size (from 0.76 to 0.18  $\mu$ m). Although the samples show aggregated morphology with  $GdFe_2O_3$  co-crystallized as secondary phase, the product could be a candidate for microwave absorption. On the other hand, Almessiere et al. introduced  $Dy^{3+}$  in  $Mn_{0.5}Zn_{0.5}Fe_2O_4$  powder (Almessiere et al., 2020). Pure single-phase crystals with cubic morphology were obtained. The addition of more Dy increases the particle size (from 11.0 to 18.2 nm), saturation magnetization (from 54.77 to 59.55 emu/g) while the value of coercivity falls drastically. It was decided that the particle size is relative to the magnetic domain, as size increases due to  $Dy^{3+}$  insertion, a multidomain is produced, consequently, decreasing the coercivity and magnetocrystalline anisotropy. More studies on cations

substitution in  $ZnFe_2O_4$  are worthy to explore, to tune its physicochemical properties for advanced applications.

Although the synthesis of magnetic NPs is well established, some of the chemicals involved are hazardous and expensive. However, from a green chemistry perspective, chemical hazards should be avoided or minimized during synthesis or other chemical processes (Anastas and Eghbali, 2010). Biological systems such as bacteria, fungi, actinomycetes, yeasts, viruses, and plant have been reported to synthesize various metal and metal oxide nanoparticles. Among these, biosynthesis of nanoparticles from plant seems to be a very effective method in developing a rapid, clean, nontoxic, and eco-friendly technology (Akhtar et al., 2013). Biogenic synthesis of NPs is a facile emerging technology that is not only eco-friendly but can potentially boost sustainable agriculture (Tovar et al., 2020). Materials produced biogenically are non-toxic, biocompatible, and environmentally benign (Aisida et al., 2020). *Moringa oleifera* is an important medicinal plant. The leaf extract contains polyphenol which serves as a natural reducing and capping agent. Therefore, providing an alternative method to the chemical synthesis of magnetic NPs (Venkateswarlu et al., 2015; Madubuonu et al., 2019; Kgatitsoe, 2018; Smaranika et al., 2013). Many magnetic NPs have been synthesized biogenically such as  $Ni/Fe_3O_4$  (Prasad et al., 2017),  $ZnFe_2O_4$  (Matinise et al., 2018) and  $Fe_3O_4$  (Sharma et al., 2019).

Reports on the biogenic synthesis of substituted zinc ferrites are rarely found in the literature. In this regard, the current paper is aimed to investigate the influence of Zn insertion into Ca-Mg spinel ferrite (as  $Zn_xCa_{0.5-x/2}Mg_{0.5-x/2}Fe_2O_4$ ) on the chemical structure and physical property of the products. Initially, the precursor gel is obtained biogenically using *Moringa oleifera* leaf extracts and crystallizes via two different methods viz: so-gel and ultrasonic methods. The physicochemical properties of the two sets of the products are compared and investigated systematically.

## 2. Experimental details

### 2.1. *Moringa oleifera* leaf collection and extraction

Dried *Moringa oleifera* leaf (originally imported from India) was collected from local markets as seen in Fig. 1. 10 mg of leaf

was crushed and mixed with 100 ml of deionized water under stirring at 60 °C for 1 h until getting the brown solution. The resulting solution was filtered by filtered papers to remove any small particles to obtain a clear brown solution.

### 2.2. Chemicals and instrumentation

All materials ( $Zn(NO_3)_2$ ,  $Mg(NO_3)_2$ ,  $Ca(NO_3)_2$ , and  $Fe(NO_3)_3 \cdot 9H_2O$ ) were analytical grade received from Merck and used without further purification.

The phase analyses of both group A and B NSF's proceeded with X-ray diffraction (Benchtop Rigaku Miniflex with Cu K $\alpha$  line). The surface analysis was analyzed by scanning and transmission electron microscope (FEI Titan ST equipped with an EDX spectrometer). An FT-IR spectrophotometer (Bruker,  $\alpha$ -II) with an attenuated total reflectance (ATR) mode for spectral analysis. Quantum Design PPMS DynaCool-9 coupled with vibrating sample magnetometer (VSM) head was utilized for magnetic measurements.

### 2.3. Synthesis $Zn_xCa_{0.5-x/2}Mg_{0.5-x/2}Fe_2O_4$ ( $x = 0.0 - 0.6$ ) NSF's

The  $Zn_xCa_{0.5-x/2}Mg_{0.5-x/2}Fe_2O_4$  ( $x = 0.0 - 0.6$ ) NSF's were fabricated by Ultrasound approach with (group A) and without (group B) *Moringa oleifera* leaf extract. The first patch was prepared by mixing a specific weight of  $Zn(NO_3)_2$ ,  $Mg(NO_3)_2$ ,  $Ca(NO_3)_2$  and  $Fe(NO_3)_3 \cdot 9H_2O$  in 50 ml of *Moringa oleifera* leaf extraction with stirring at 80 °C for 30 min. The solution was exposed to Ultrasonic Homogenizer for 40 min and 20 kHz, after that the mixture was heated up at 350 °C until burn and turn to black powder. The second patch was synthesized with the stoichiometric mixture of  $Zn(NO_3)_2$ ,  $Mg(NO_3)_2$ ,  $Ca(NO_3)_2$  and  $Fe(NO_3)_3 \cdot 9H_2O$  in 50 ml deionized water with stirring without adding *Moringa oleifera* leaf extract, subsequently, there pH was attuned at 11 via 2 M NaOH solution then undergoes to ultrasonic homogenizer for 40 min and 20 kHz. The powder was washed on deionized water 3–5 times until reach neutral pH, then dried in an open oven at 60 °C overnight to achieved NSF's. Finally, both group A and B NSF's were calcinated at 600 °C for 4 h.

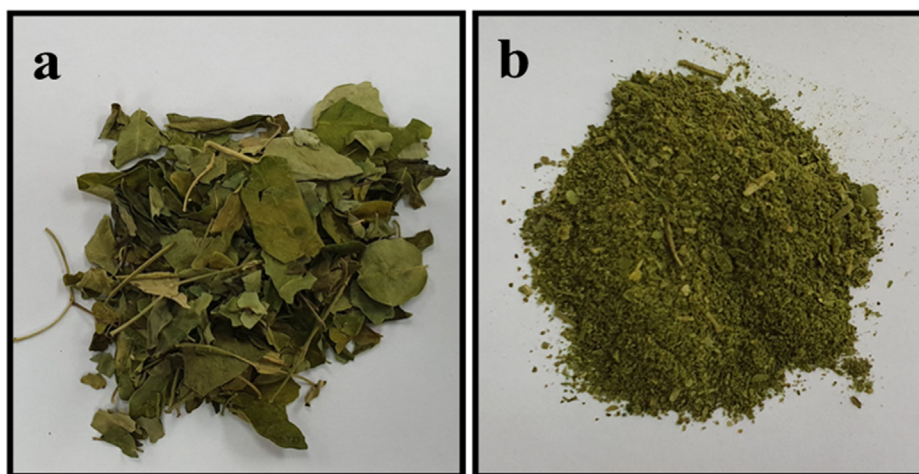


**Fig. 1** *Moringa oleifera* leaf before and after crushing.

### 3. Results and discussion

#### 3.1. Microstructure

XRD powder patterns of  $Zn_xCa_{0.5-x/2}Mg_{0.5-x/2}Fe_2O_4$  ( $x = 0.0 - 0.6$ ) NSFs for group A and B are presented in Fig. 2. All characteristic peaks in both diffraction patterns are matched with cubic spinel structure without detecting any type of impurity confirming the efficiency of the synthesized method. The broad peaks in the XRD powder patterns indicated the small crystallite size. The structure parameters were extracted by Rietveld refinement (Match3! and full proof) using XRD powder pattern experimental data as listed in Table 1. It was found that the lattice parameters ( $a_0$ ) were increased when increased the ratio Zn in both compositions due to the expansion into the spinel lattice. Likewise, the crystal size was increased with increasing Zn content, but the crystal size of group A is smaller than the group B NSFs.

Well-known Bertaut method has been utilized to calculate the cation occupancy (Shirsath et al., 2013) of cations in  $Zn_xCa_{0.5-x/2}Mg_{0.5-x/2}Fe_2O_4$  ( $x = 0.0 - 0.6$ ) NSFs for group A and B. The ratio of the intensities of  $I_{220}/I_{440}$  and  $I_{422}/I_{400}$  planes were used for the cation distribution calculations (Shirsath et al., 2014). This method selects a few pairs of reflections according to the expression;

$$\frac{I_{hkl}^{Obs.}}{I_{h'k'l'}^{Obs.}} \propto \frac{I_{hkl}^{Calc.}}{I_{h'k'l'}^{Calc.}} \quad (1)$$

where  $I_{hkl}^{Obs.}$  and  $I_{hkl}^{Calc.}$  are the observed and calculated intensities for reflection  $(hkl)$ , respectively. In this method the best information on cation distribution is achieved when comparing experimental and calculated intensity ratios for reflections whose intensities (i) are nearly independent of the oxygen parameter, (ii) vary with the cation distribution in opposite ways and (iii) do not differ significantly. If an agreement factor ( $R$ ) is defined as in Eq. (2), the best-simulated structure which matches the actual structure of the sample will lead to a

minimum value of  $R$  and the corresponding cation distribution is obtained for each  $hkl$  and  $h'k'l'$  reflection pair considered.

$$R = \left| \left( \frac{I_{hkl}^{Obs.}}{I_{h'k'l'}^{Obs.}} \right) - \left( \frac{I_{hkl}^{Calc.}}{I_{h'k'l'}^{Calc.}} \right) \right| \quad (2)$$

The intensities of these are nearly independent of the oxygen parameters. The calculations were made for various combinations of cations. The above-mentioned intensity ratios expected for given arrangements of the cations and compare them with the experimental values. The relative integrated intensity of a given diffraction line from powder specimens as observed in a diffractometer with a flat-plate sample holder, the following formula is valid;

$$I_{hkl} = |F|_{hkl}^2 P \cdot L_P \quad (3)$$

where  $P$  is multiplicity factor,  $F$  is structure factor,  $L_P$  the Lorentz polarization factor which is,

$$L_P = \frac{1 + \cos^2 2\theta}{\sin^2 \cos 2\theta} \quad (4)$$

The atomic scattering factor for various ions was taken from the literature (Cullity, 1972). The cation distribution calculated by this method is shown in Table 1.  $Zn^{2+}$  ions show their preference to occupy the  $T_d$  site for both group A and B (Shirsath et al., 2018). In both groups,  $Ca^{2+}$  and  $Mg^{2+}$  ions occupy B-site only.  $Fe^{3+}$  ions are distributed over both  $T_d$  and  $O_h$  sites, however, the most of these ions occupy the B site.

#### 3.2. Electron microscopy

Fig. 3 exhibited the SEM images of  $Zn_xCa_{0.5-x/2}Mg_{0.5-x/2}Fe_2O_4$  ( $x = 0.0 - 0.6$ ) NSFs prepared using green synthesis (group A) and with Ultrasound irradiation (group B). Group A samples were showed highly agglomeration of very fine spherical particles with uniform distribution and some individual particles are obviously visible due to the effect of biosynthesis. While group B presented agglomerated particles of inhomogeneous

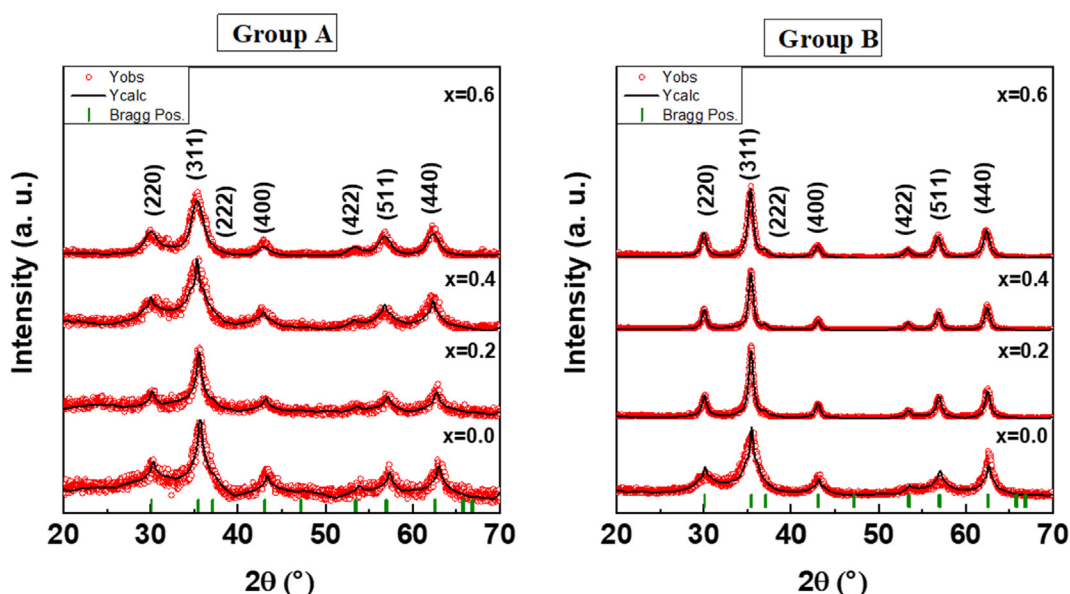


**Fig. 2** XRD powder patterns of  $Zn_xCa_{0.5-x/2}Mg_{0.5-x/2}Fe_2O_4$  ( $x = 0.0 - 0.6$ ) NSFs for groups A and B.

**Table 1** The refined cell parameters of  $Zn_xCa_{0.5-x/2}Mg_{0.5-x/2}Fe_2O_4$  ( $x = 0.0 - 0.6$ ) NSFs for group A and B.

Group A							
X	$a$ (Å)	$V$ (Å) <sup>3</sup>	$D_{XRD}$ (nm) $\pm$ 0.06	$\chi^2(chi^2)$	$R_{Bragg}$	Cation distribution	
						A-site	B-site
0.0	8.3973	592.141	10.6	1.5	25.6	Fe <sub>0.20</sub>	Ca <sub>0.5</sub> Mg <sub>0.5</sub> Fe <sub>1.8</sub>
0.2	8.4008	592.862	12.4	0.9	12.2	Zn <sub>0.2</sub> Fe <sub>0.18</sub>	Ca <sub>0.4</sub> Mg <sub>0.4</sub> Fe <sub>1.82</sub>
0.4	8.4250	598.005	15.7	1.2	16.3	Zn <sub>0.4</sub> Fe <sub>0.1.9</sub>	Ca <sub>0.3</sub> Mg <sub>0.3</sub> Fe <sub>1.81</sub>
0.6	8.4276	598.569	17.4	1.3	16.2	Zn <sub>0.6</sub> Fe <sub>0.20</sub>	Ca <sub>0.2</sub> Mg <sub>0.2</sub> Fe <sub>1.8</sub>
Group B							
x	$a$ (Å)	$V$ (Å) <sup>3</sup>	$D_{XRD}$ (nm) $\pm$ 0.06	$\chi^2(chi^2)$	$R_{Bragg}$	Cation distribution	
						A-site	B-site
0.0	8.3903	590.661	16.4	1.6	17.9	Fe <sub>0.20</sub>	Ca <sub>0.5</sub> Mg <sub>0.5</sub> Fe <sub>1.8</sub>
0.2	8.4067	594.119	24.3	1.3	10.5	Zn <sub>0.2</sub> Fe <sub>0.19</sub>	Ca <sub>0.4</sub> Mg <sub>0.4</sub> Fe <sub>1.8</sub>
0.4	8.4114	595.109	26.6	1.1	7.5	Zn <sub>0.4</sub> Fe <sub>0.1.8</sub>	Ca <sub>0.3</sub> Mg <sub>0.3</sub> Fe <sub>1.8</sub>
0.6	8.4199	596.934	28.0	1.5	8.8	Zn <sub>0.6</sub> Fe <sub>0.20</sub>	Ca <sub>0.2</sub> Mg <sub>0.2</sub> Fe <sub>1.8</sub>

size distribution. The agglomeration in both groups was due to highly energies magnetic between particles. However, the NSFs of group B were revealed also a high aggregation of little big spherical and cubic particles because of the magnetic interaction between these particles. These observations were confirmed via TEM as seen in Fig. 4. This approves that the green synthesis offered a homogeneous dispersed with narrowly size distribution around 18 nm for group A and nearly to 30 nm for group B. The elemental analysis of  $Zn_xCa_{0.5-x/2}Mg_{0.5-x/2}Fe_2O_4$  ( $x = 0.4$ ) group A and with Ultrasound irradiation (group B) were estimated via EDX elemental and mapping as clear from Fig. 5. The EDX spectra substantiated the existence of Zn, Ca, Mg, O and Fe elements which showed the effectiveness of the synthesis method.

### 3.3. Spectral investigation

Fig. 6 represented FT-IR spectra of  $Zn_xCa_{0.5-x/2}Mg_{0.5-x/2}Fe_2O_4$  ( $x = 0.0 - 0.6$ ) NSFs of group A and B. The spectra of all samples revealed the index vibration modes of cubic spinel ferrite at 401 and 540 cm<sup>-1</sup> due to stretching vibration of metal–oxygen bond in the octahedral site and tetrahedral sites correspondingly. Moreover, it is clear that there is a shift towards high frequency with increasing the Zn ratio caused by differences in the distance between metal–oxygen band for T<sub>d</sub> and O<sub>h</sub> site jointly via changing the amount of Zn (Ahmad et al., 2018). However, the NSFs of group A presented vibration mode at 1116 cm<sup>-1</sup> relevant to stretching vibrations of C—O—C and C—O (Waldron, 1955). The Moringa leaves are known as a rich source of vitamins, polyphenols, iron, calcium, folic acid and beta-carotene. Previous reports have studied the spectrum of Moringa leaf extract that showed various absorption peaks indicating the presence of the hydroxyl functional group in alcohols and phenolic compounds (Sutherland et al., 1994; Ndabigengesere et al., 1995; Sathyavathi et al., 2011). The several bands were found indicative of alkane C—H stretch, which is owed to the lipid molecules in the leaf broth. The presence of vibration of —C O, has been also demonstrated and associated with amide II bond from proteins, whereas —C—O—, —C—C— stretches linked to lipids and sugars. It was observed that the bands due to C—H

stretch, C≡C, nitro compounds, amine (C—N) stretch, and phenyl (C—H) stretch were missing completely during the reduction of metal ions to nanoparticles. Such studies suggest the binding of protein present in the extract with nanoparticles through free carboxylate group and additionally few of the bio-organics from *moringa oleifera* constitutes a strong coating/capping on the synthesized nanoparticles.

### 3.4. VSM measurements

The magnetic features of the produced  $Zn_xCa_{0.5-x/2}Mg_{0.5-x/2}Fe_2O_4$  ( $x = 0.0 - 0.6$ ) NSFs for group A and B have been investigated at room (T = 300 K) and low (T = 10 K) temperatures by means of VSM instrument under an applied magnetic field (H) varying from −70 to +70 kOe. Magnetic hysteresis plots, illustrating the variations of magnetization versus the magnetic field, for various prepared samples are presented in Figs. 7 and 8. The various deduced magnetic parameters are illustrated in Fig. 9.

The non-substituted  $Ca_{0.5}Mg_{0.5}Fe_2O_4$  (i.e.  $x = 0.0$ ) NSFs of group A and B are soft magnetic materials at RT. Similarly, the samples of Zn substituted CaMg NSFs of group A and B are soft magnetic materials at 300 K. All samples displayed SPM (superparamagnetic) behavior at room temperature, with no or negligible coercivity and retentivity. The room temperature SPM behavior of the prepared NPs was studied, considering the values of magnetic squareness ratio (SQR = M<sub>r</sub>/M<sub>s</sub>), which are presented in Fig. 9(e). When the SQR value is lower than 0.1, it means that higher than 90% of the magnetization has been lost once the external magnetic field is removed. At room temperature, the determined SQR values reveal that all NSFs of group A and B are SPM at T = 300 K, displaying low or negligible H<sub>c</sub> and M<sub>r</sub> values. The noticed SPM behavior is happened owing to the thermal effects in the products. In these SPM nanoparticles, the thermal fluctuations are strong enough to spontaneously demagnetize a previously saturated assembly (Sulaiman et al., 2018; Slimani et al., 2019). This observed characteristic is believed to be a great magnetic feature, and the SPM behavior of  $Zn_xCa_{0.5-x/2}Mg_{0.5-x/2}Fe_2O_4$  ( $x = 0.0-0.6$ ) NSFs is apparent in different cases at room temperature. The benefit of SPM ferrites is correlated to their

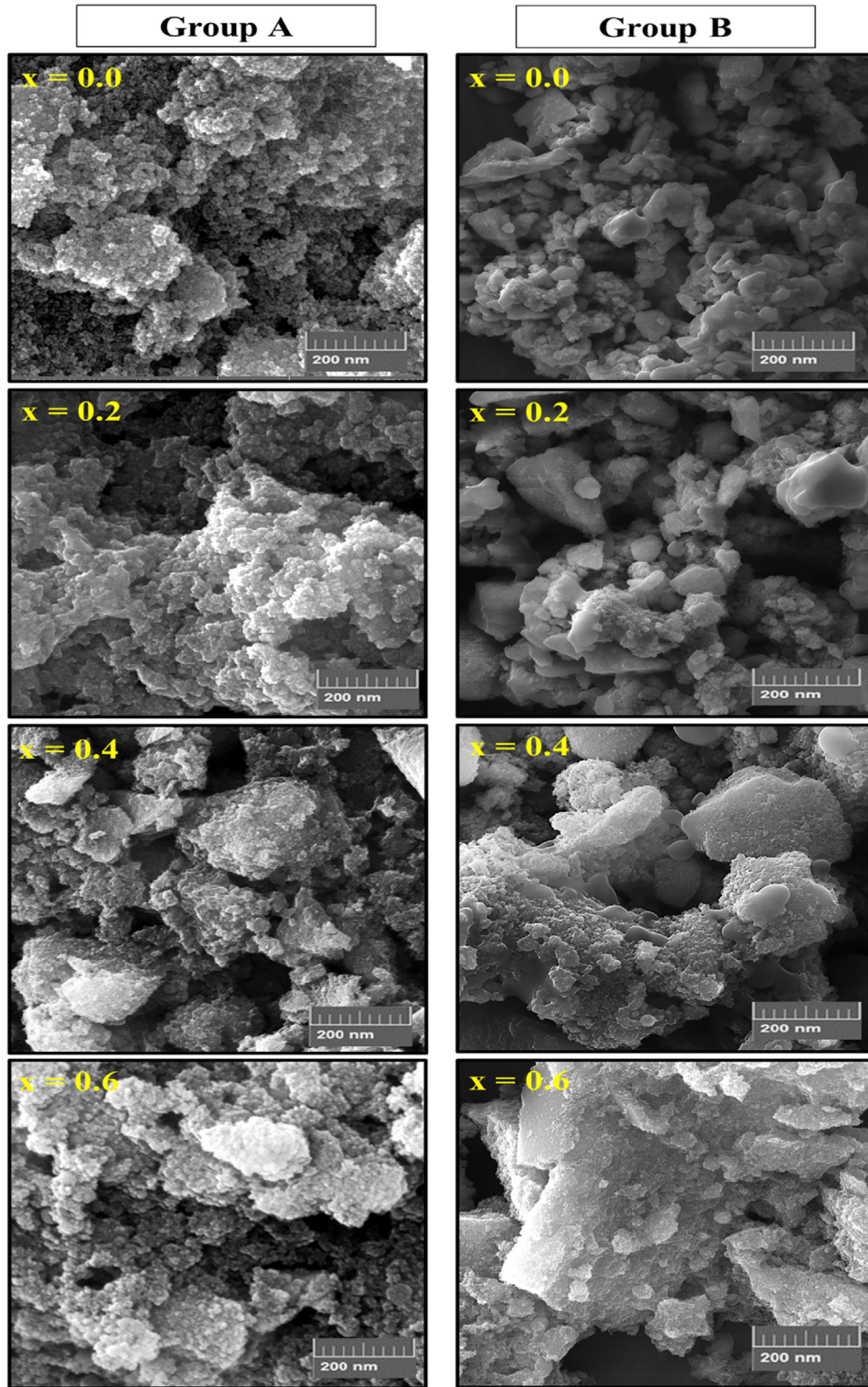


**Fig. 3** SEM images of  $Zn_xCa_{0.5-x/2}Mg_{0.5-x/2}Fe_2O_4$  ( $x = 0.0\text{--}0.6$ ) NSF s of groups A and B.

highly sensitive response to an external magnetic field. Such property makes these magnetic NSF s promising candidates for various applications, especially in biomedical areas, like in cell separation and detection, in supporting gene delivery, in cell diagnostics using magnetic resonance imaging (MRI), as well as for anti-bacterial and anti-cancer activities (Yunas

et al., 2018; Almessiere et al., 2020; Elayakumar et al., 2019; Akhtar et al., 2019). These prospective applications show that the enhanced performances of the superparamagnetic nanoparticles will find vital role in developing forthcoming biomedical technologies particularly for the targeting drugs, therapy, as well as for diagnostics purposes. Moreover, such

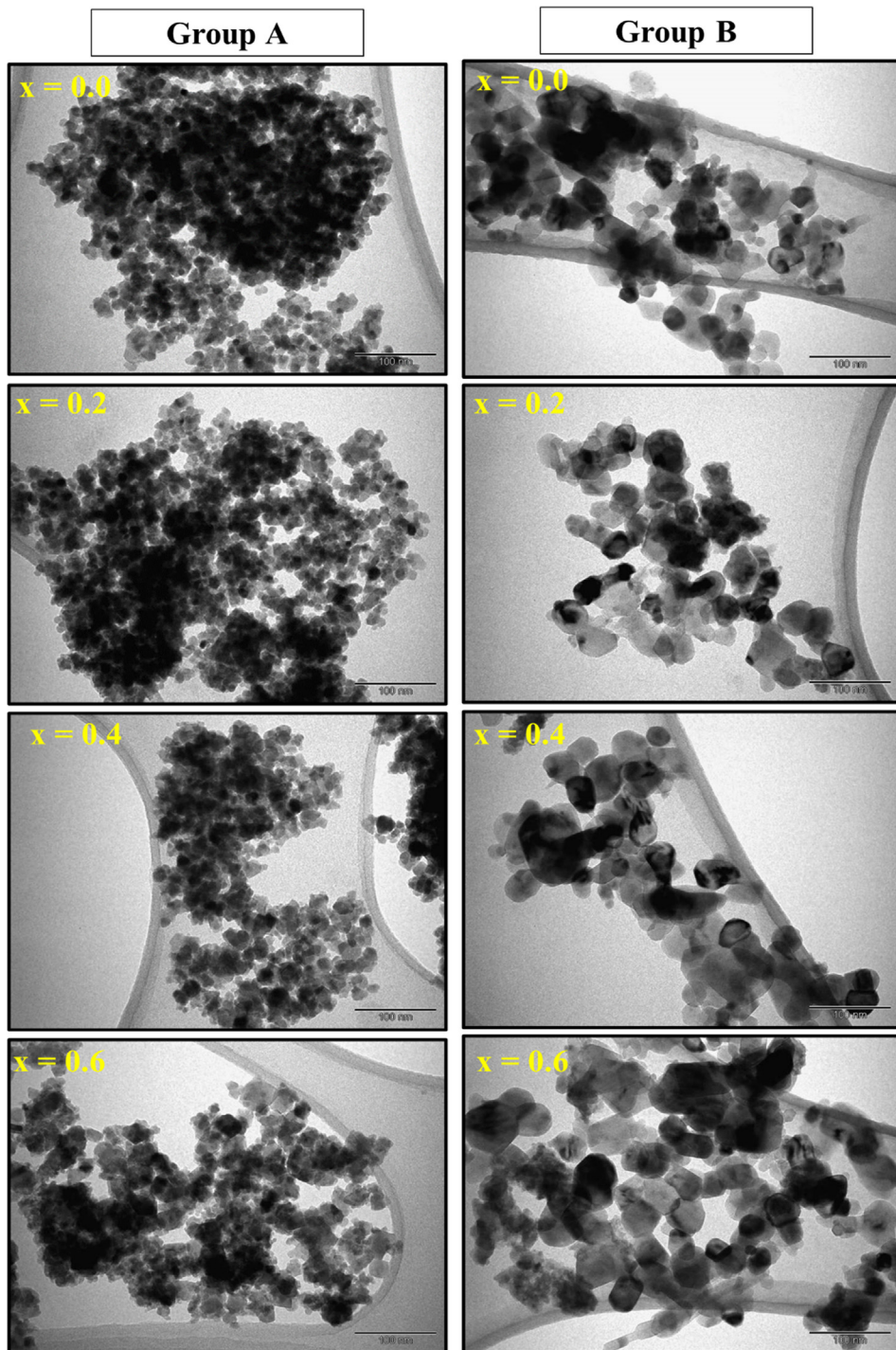


**Fig. 4** TEM images of  $Zn_xCa_{0.5-x/2}Mg_{0.5-x/2}Fe_2O_4$  ( $x = 0.0\text{--}0.6$ ) NSFs of groups A and B.

superparamagnetic NPs could be also employed for the transportation of drug in blood vessels as well as magnetic drug carriers in drug delivery applications, and for the creation of a localized heating effect for selective cancer cells treatments. Nevertheless, the different samples revealed opened M–H hysteresis loops at a temperature of 10 K, which indicates their ferromagnetic (FM) behavior at very low temperatures. As discussed above, a SQR value lower than 0.1 reflects a superparamagnetic behavior. When the SQR is higher than

0.1, this would indicate that the prepared nanoparticles are ferro/ferri-magnetic. It is clear from Fig. 9(e) that the SQR values are higher than 0.1 for all samples at 10 K. This finding confirms the observed ferromagnetic behavior at 10 K for all products. Furthermore, it has been established that the NPs consist of single-magnetic domain for  $x > 0.5$  and of multi-magnetic domain for  $x < 0.5$  (Akhtar et al., 2019; Slimani et al., 2019). In the present study, SQR values at 10 K for all NSFs of group A and B are between 0.2 and 0.3, which is

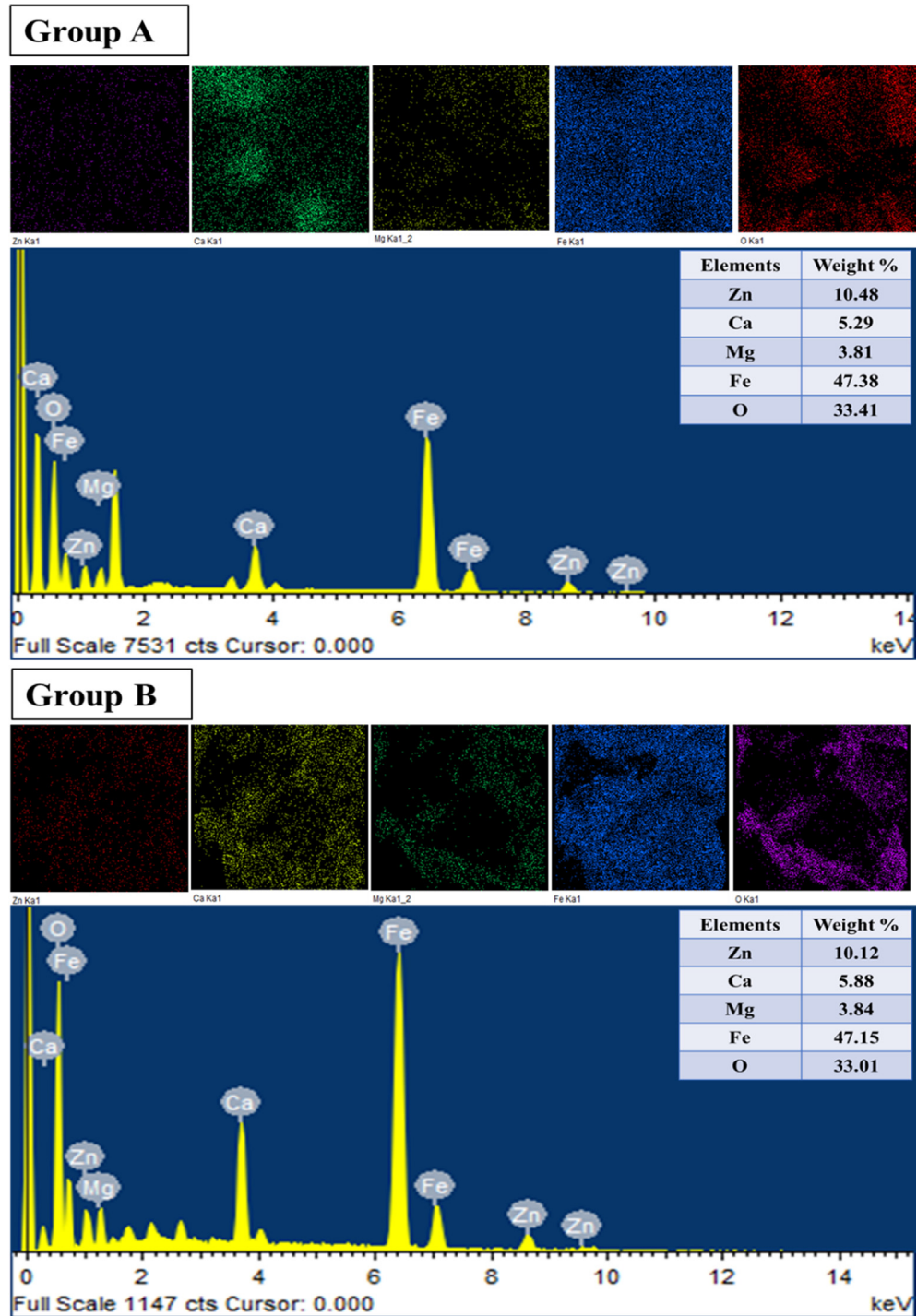


Fig. 5 EDX and elemental mapping of  $Zn_xCa_{0.5-x/2}Mg_{0.5-x/2}Fe_2O_4$  ( $x = 0.4$ ) NSF samples of groups A and B.

below the theoretical limit of 0.5, reflecting the NPs consist of multi-magnetic domains.

The values of  $M_s$  for all NSFs of both groups A and B are much greater at 10 K than those at 300 K. Such trend is a feature of tiny nanoparticles in accordance with the relationship among the thermal energy  $k_B T$  and the anisotropy energy  $KV$ . Here,  $T$  is the temperature,  $k_B$  is the Boltzmann constant,  $V$  is the nanoparticle's volume, and  $K$  is the anisotropy constant. The dissimilar values of  $M_s$  at 300 and 10 K are thought

to reveal the small impact of thermal fluctuation since the particles are nanoscopic. This is reasonable since the thermal fluctuations are being smaller at lower temperatures. The magnetic features at room and low temperatures were found to be analogous to those studied for  $Mg_{1-x}Zn_xFe_2O_4$  NPs synthesized through wet chemical approach (Kondo et al., 2013).

It is clear from Figs. 7, 8 and 9(a) that the  $Zn_xCa_{0.5-x/2}Mg_{0.5-x/2}Fe_2O_4$  ( $x = 0.0-0.6$ ) NSFs prepared using *Moringa oleifera* extract (Group A samples) displayed lower  $M_s$  values

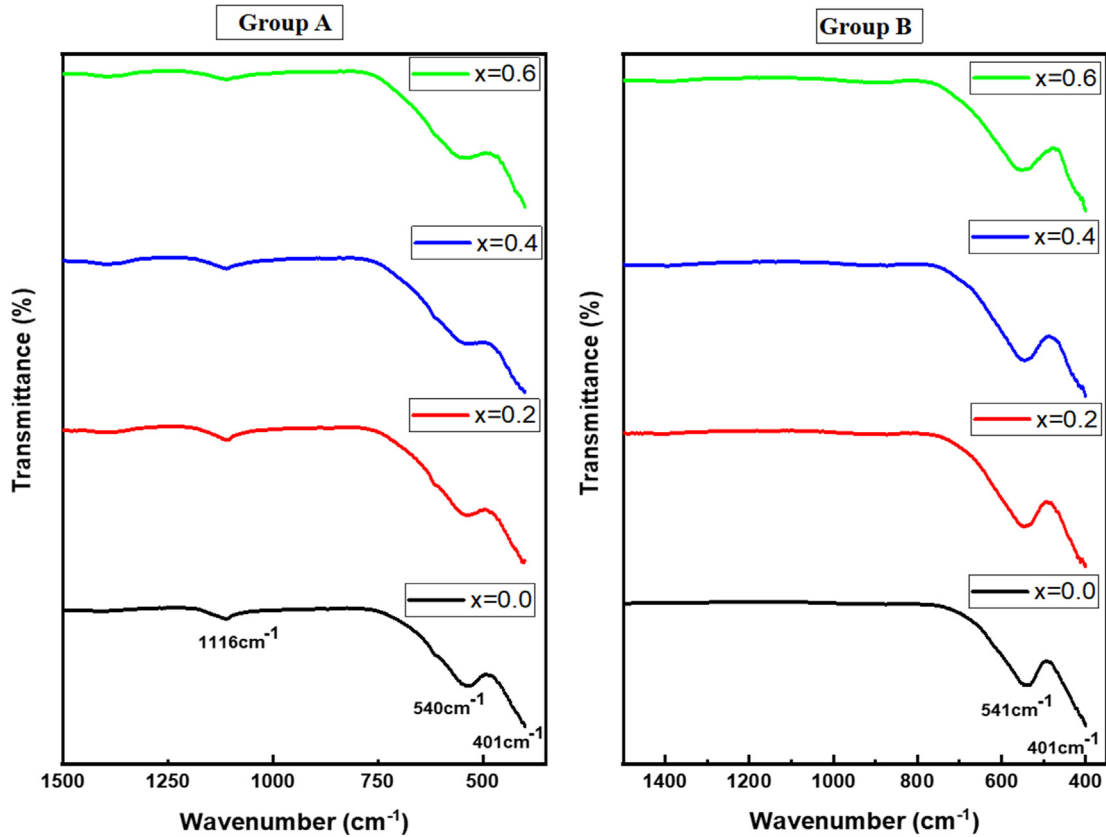


**Fig. 6** FT-IR spectra of  $Zn_xCa_{0.5-x/2}Mg_{0.5-x/2}Fe_2O_4$  ( $x = 0.0\text{--}0.6$ ) NSF samples of groups A and B.

in comparison to those in NSF prepared without using *Moringa oleifera* extract (Group B samples). According to the above performed structural (crystallites size) and morphological (particles size) investigations, Group A samples exhibited very small particles size compared to Group B samples. With decreasing particles size, the effects of spin canting and thermal changes will more efficient and hence provoke a reduction in the value of magnetic saturation (Murugesan and Chandrasekaran, 2015; Slimani et al., 2019). In line with this finding, it was expected that samples prepared using *Moringa oleifera* extract (Group A samples) will display lower magnetization values in comparison to those in samples prepared without using *Moringa oleifera* extract (Group B samples). Moreover, FT-IR spectra showed vibration bonds relevant to stretching vibrations of C—O—C and C—O. It is widely reported that the inclusion of carbon-based materials results in a quantitative reduction of magnetization without altering the magnetic ordering (Gunasekaran et al., 2021). In fact, when the  $Zn_xCa_{0.5-x/2}Mg_{0.5-x/2}Fe_2O_4$  ( $x = 0.0\text{--}0.6$ ) NSF are incorporated by a low-magnetic or non-magnetic matrix such as carbon, carbon nanotubes, graphene oxide, etc., the carbons pertain their self as a host in arresting the ferrite nanoparticles, which will hinder the growth of ferrite nanoparticles, and hence decreasing their size dimensional drastically (which is already shown from structural and morphological examinations). The diminution in particles size as well as the non-magnetic or low-magnetic carbon-matrix will results in lessening the magnitude of magnetization.

On the other hand, it was clear that that the substitution and the increase of  $Zn^{2+}$  ions within the CaMg spinel ferrites

caused a great variation in the magnetic parameters such as the  $M_s$  and  $H_c$  values as shown in Fig. 9. The magnetic features of  $Zn^{2+}$  substituted CaMg spinel ferrite NPs ( $Zn_xCa_{0.5-x/2}Mg_{0.5-x/2}Fe_2O_4$ ) highlight that the co-substitution of Mg and Ca by Zn into the spinel structure display linear effects on the  $M_s$  and  $H_c$  values. It is seen that the  $M_s$  values of the  $Zn_xCa_{0.5-x/2}Mg_{0.5-x/2}Fe_2O_4$  ( $x = 0.0\text{--}0.6$ ) NSF of group A and B progressively intensified with the rise of Zn doping content up to  $x = 0.6$  (Fig. 9(a)). Therefore, the saturation magnetization of  $Zn_xCa_{0.5-x/2}Mg_{0.5-x/2}Fe_2O_4$  ( $x = 0.0\text{--}0.6$ ) NSF of group A and B is depending mainly on the distribution of  $Fe^{3+}$  ions between the tetrahedral ( $T_d$ ) and octahedral ( $O_h$ ) sites, since the different other ions  $Zn^{2+}$ ,  $Ca^{2+}$ , and  $Mg^{2+}$  are naturally non-magnetic ions, while the magnetic moment of  $Fe^{3+}$  ions is equal to  $5 \mu_B$ . The different produced  $Zn_xCa_{0.5-x/2}Mg_{0.5-x/2}Fe_2O_4$  ( $x = 0.0\text{--}0.6$ ) NSF displayed superparamagnetic (SPM) behavior. This implies that the ions of  $Ca^{2+}$  and  $Mg^{2+}$  reside either in  $T_d$  and/or  $O_h$  sites, and the ions of  $Fe^{3+}$  at both the  $T_d$  and  $O_h$  sites, while the dopant ions of  $Zn^{2+}$  reside in the  $T_d$  sites (Manikandan et al., 2013), hence presenting SPM behavior. Similar findings were founded in the literature (Manikandan et al., 2013). The  $M_s$  values achieved maximum values of 51.68 emu/g at 300 K and 96.97 emu/g at 10 K for samples with  $x$  content of 0.6 of group B. Similarly, the maximum  $M_s$  values are attained for NSF with  $x = 0.6$  of group A with values of 24.50 emu/g at 300 K and 63.45 emu/g at 10 K. In any case, whatever using *Moringa oleifera* extraction or without, the obtained  $M_s$  values in the present study are higher in comparison to those previously registered in nanoparticles of Ca spinel ferrite

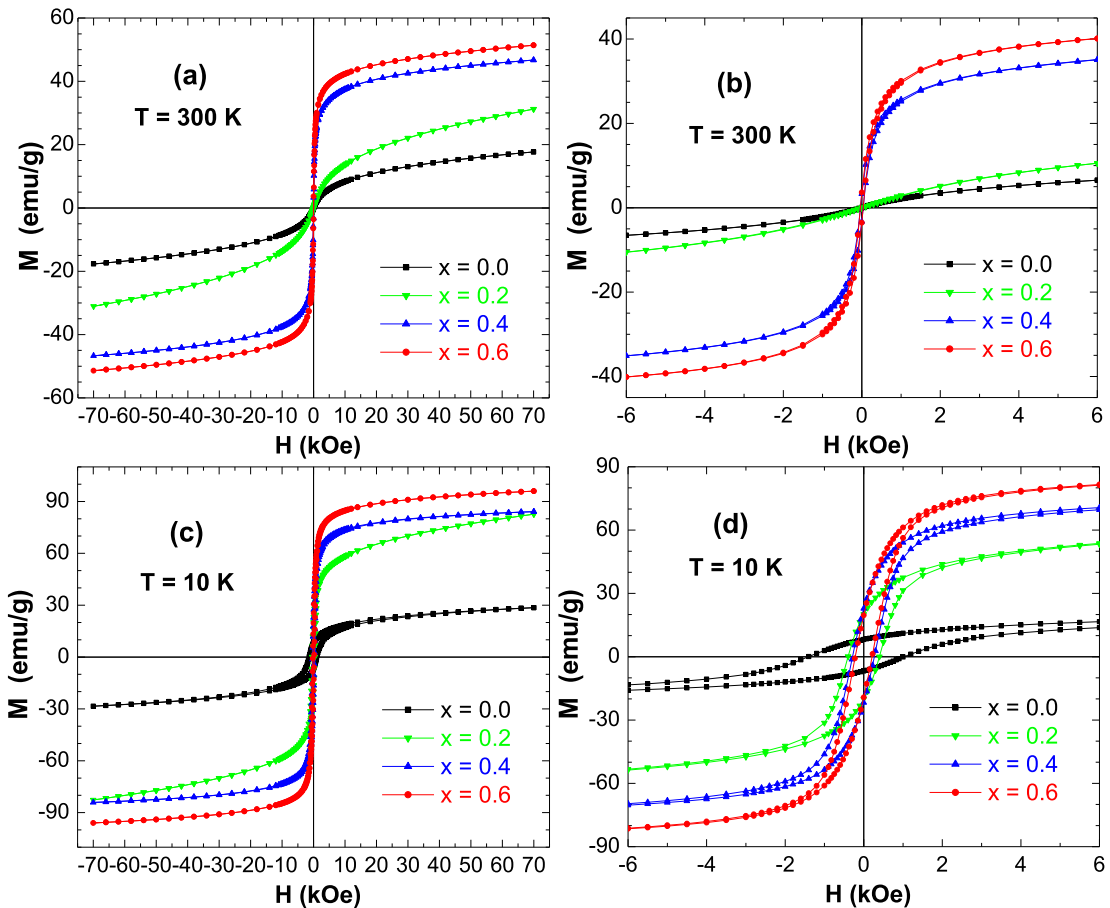


**Fig. 7** M–H curves performed at (a,b) T = 300 K and (c,d) T = 10 K for  $Zn_xCa_{0.5-x/2}Mg_{0.5-x/2}Fe_2O_4$  ( $x = 0.0 – 0.6$ ) NSF s prepared without *Moringa oleifera* extract (Group B samples). The Figures (b) and (d) are enlarged views of Figures (a) and (c) near to  $H = 0$  kOe, respectively.

(12.8 emu/g (Pereira, 2019), Mg spinel ferrite (16.1 emu/g (Cardoso et al., 2018), and Zn spinel ferrite (~7 emu/g (Mozaffari et al., 2010). The  $M_s$  value of 51.68 emu/g attained at room temperature in the  $Zn_{0.6}Ca_{0.2}Mg_{0.2}Fe_2O_4$  NSF s of group B is greater than the  $M_s$  value of about 48.5 emu/g in Mn spinel ferrite nanofibers produced via electrospinning technique (Abraham et al., 2019), 30.5 emu/g in Mg spinel ferrite NPs prepared through sol–gel combustion procedure (Huang et al., 2006), and 14.1 emu/g in Mg spinel ferrite NPs prepared through co-precipitation process (Rashad, 2007). The  $M_s$  value of 24.5 emu/g reached at room temperature for  $Zn_{0.6}Ca_{0.2}-Mg_{0.2}Fe_2O_4$  NSF s of group A is greater than the  $M_s$  of 7.1 emu/g found in  $ZnFe_2O_4$  synthesized via aloe vera plants extraction assisted hydrothermal technique (Phumying et al., 2013), 14.8 emu/g for  $Mg_{0.85}Zn_{0.15}Fe_2O_4$  nanoparticles prepared via the modified sol–gel approach using aloe vera plants extraction (Dora et al., 2014), 12.1 emu/g for  $ZnO-CoFe_2O_4$  synthesized through the hydrothermal technique via the use of rambutan peel (*Nephelium lappaceum L.*) extraction (Rahmayeni et al., 2019).

The growth of  $M_s$  values with rising  $Zn^{2+}$  content is caused by the misbalance of the ions of  $Fe^{3+}$   $T_d$  and  $O_h$  sites, the non-collinear nature of moments in the  $O_h$  site and the variations in super-exchange interactions, which cause the intensification of the net magnetization (Ramarao et al., 2018). For instance,

$ZnMg$  ferrite nanoparticles were produced via co-precipitation process by Rahman et al. (2013). It was found an increase in the values of  $M_s$ . Manikandan et al. (2013) investigated the magnetic features of  $ZnMg$  ferrites nanoparticles fabricated through rapid microwave combustion approach and they reported an enhancement in  $M_s$  values. Ramarao et al. (2018) synthesized  $Mg_{1-x}Zn_xFe_2O_4$  ( $x = 0.0–0.3$ ) via conventional ceramic route. They indicated that  $M_s$  value rises with the increase in the Zn content. Kondo et al. (2013) produced nanoparticles of  $Zn_xMg_{1-x}Fe_2O_4$  ( $x = 0.0–0.8$ ) via a wet chemical process. They found that  $M_s$  value increases with Zn doping content up to  $x = 0.4$  concentration and then starts to decrease with further increasing Zn content.

At both temperatures (300 and 10 K), the  $M_s$  values of various  $Zn_xCa_{0.5-x/2}Mg_{0.5-x/2}Fe_2O_4$  ( $x = 0.0 – 0.6$ ) NSF s are increasing with rising the content of  $Zn^{2+}$  ions in  $Ca_{0.5}Mg_{0.5}-Fe_2O_4$  lattice. This is mostly attributed to the doping with  $Zn^{2+}$  ions that have the preference to lodge in the  $T_d$  sites, which will drive the  $Fe^{3+}$  ions to transfer towards the  $O_h$  site. This provides a reduction in the anti-parallel spins coupling and spins canting, causing a strengthening of A-B exchange interactions, and hence resulting in an increase in the values of  $M_s$ . The noted variations in  $M_s$  values can be explained based on the two sublattices model of proposed by Neel (Almessiere et al., 2020; Vinosha et al., 2020; Vinosha et al.,

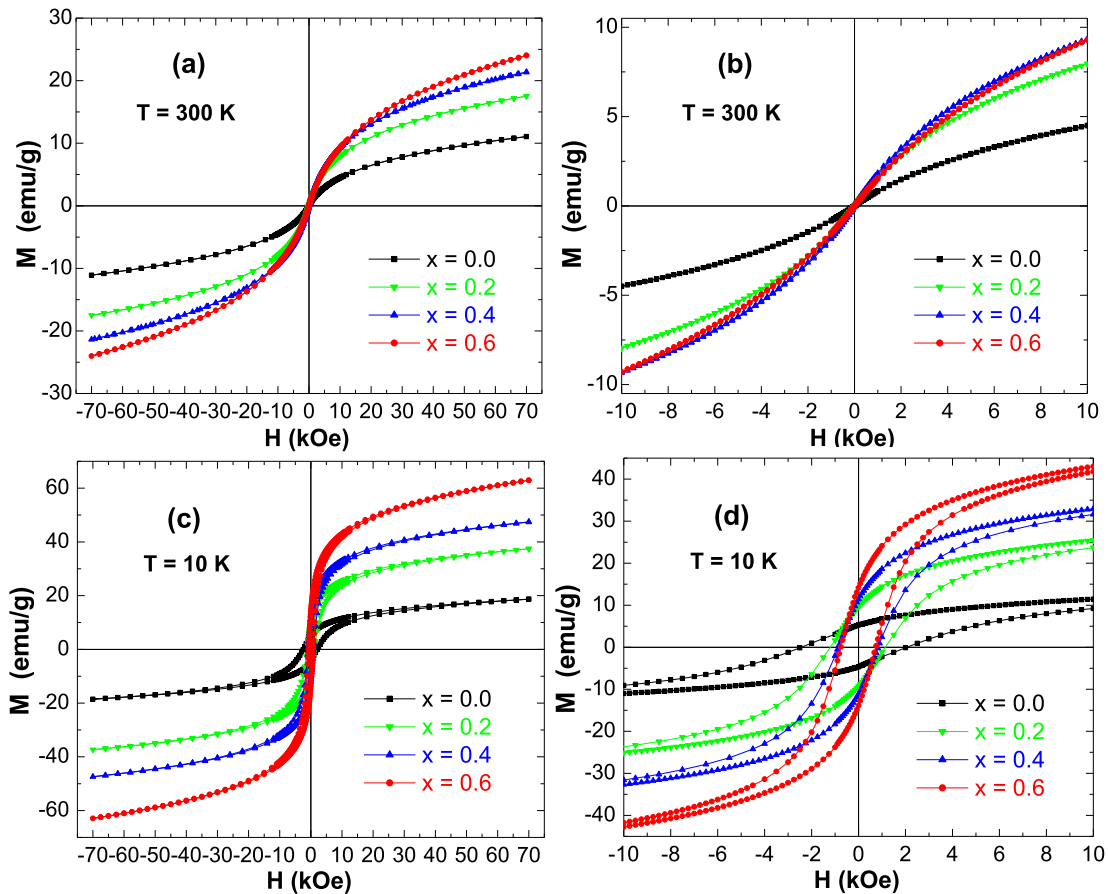


**Fig. 8** M–H curves performed at (a, b)  $T = 300\text{ K}$  and (c, d)  $T = 10\text{ K}$  for  $\text{Zn}_x\text{Ca}_{0.5-x}/2\text{Mg}_{0.5-x}/2\text{Fe}_2\text{O}_4$  ( $x = 0.0\text{--}0.6$ ) NSFs prepared with *Moringa oleifera* extract (Group A samples). The figures (b) and (d) are enlarged views of figures (a) and (c) near to  $H = 0\text{ kOe}$ , respectively.

2020). In accordance with this model, the magnetic moments at the  $T_d$  and  $O_h$  sites are antiparallel to each other. Hence, the resulting magnetic moment would depend on the difference in the magnetic moments of  $T_d$  and  $O_h$  lattices. We note that the magnetic interactions among the ions occupying the  $T_d$  (A) and  $O_h$  (B) sites are relatively stronger compared to those of ions accommodated at the identical sublattice, viz. A–A or B–B interactions. So, according to the above-mentioned model, the net magnetization ( $M$ ) could be expressed as follow:

$$M = M_B - M_A \quad (5)$$

Here,  $M_A$  and  $M_B$  are the net magnetization in  $T_d$  and  $O_h$  sublattices, respectively. Certainly, the net magnetization determines the value of  $M_s$ . The replacement of some non-magnetic or magnetic ions within the spinel lattice changes the distribution of cations. If the replaced ions display dissimilar ionic radii, this provokes a decrease or an increase in the bond lengths and bond angles, which could improve or diminish the magnetic interactions and alters the magnetic features of the spinel ferrite. In the present study, the lattice parameter ‘ $a$ ’ of various NSFs of both group A and B increased with  $\text{Zn}^{2+}$  doping and led to an expansion of the unit cell volume. This will lead to increase the inter-atomic distances among the different ions, and hence alters the magnetic features. Both structural and magnetic characteristics of CaMg NSFs are

greatly depending on  $\text{Zn}^{2+}$  ions doping content. Zn spinel ferrite is considered as a normal spinel where the nonmagnetic  $\text{Zn}^{2+}$  ions and the magnetic  $\text{Fe}^{3+}$  ions are allocated in  $T_d$  and  $O_h$  sites, respectively (Thummer et al., 2004). Whereas Mg ferrite is considered as an incomplete inverse spinel wherein the  $\text{Mg}^{2+}$  and  $\text{Fe}^{3+}$  ions occupy partially the  $T_d$  and  $O_h$  sites (Ramarao et al., 2018). Based on the literature (Lal et al., 2019), Ca ferrites have also incomplete inverse spinel structure with the preference of  $\text{Ca}^{2+}$  and  $\text{Fe}^{3+}$  ions to occupy partially the  $T_d$  and  $O_h$  sites. The different divalent ions  $\text{Ca}^{2+}$ ,  $\text{Mg}^{2+}$ , and  $\text{Zn}^{2+}$  are naturally non-magnetic ( $0\text{ }\mu_B$ ). Hence, it could be expected no variation in the  $M_s$  value with the increase of  $\text{Zn}^{2+}$  ions concentration. Contrary to this expectation, the value of  $M_s$  enhances with the Zn substitution. Accordingly, the  $M_s$  values of these spinel ferrite NPs is greatly affected by the distribution of cations on  $T_d$  and  $O_h$  lattice sites. Usually, it is thought that non-substituted Ca ferrite do not display significant magnetic performances since the B–B super-exchange interactions are dominating and the magnetic moments in the  $O_h$  sites are antiparallel to each other. In CaMg spinel ferrites, portions of  $\text{Mg}^{2+}$  ions could enter within the  $T_d$  sites. Hence, the inclusion of  $\text{Mg}^{2+}$  ions will provoke an increase in  $\text{Fe}^{3+}$  ions at  $O_h$  sites and a decrease of  $\text{Fe}^{3+}$  ions at  $T_d$  sites, strengthening the overall magnetization of the entire lattice. Consequently, the net magnetization become non-

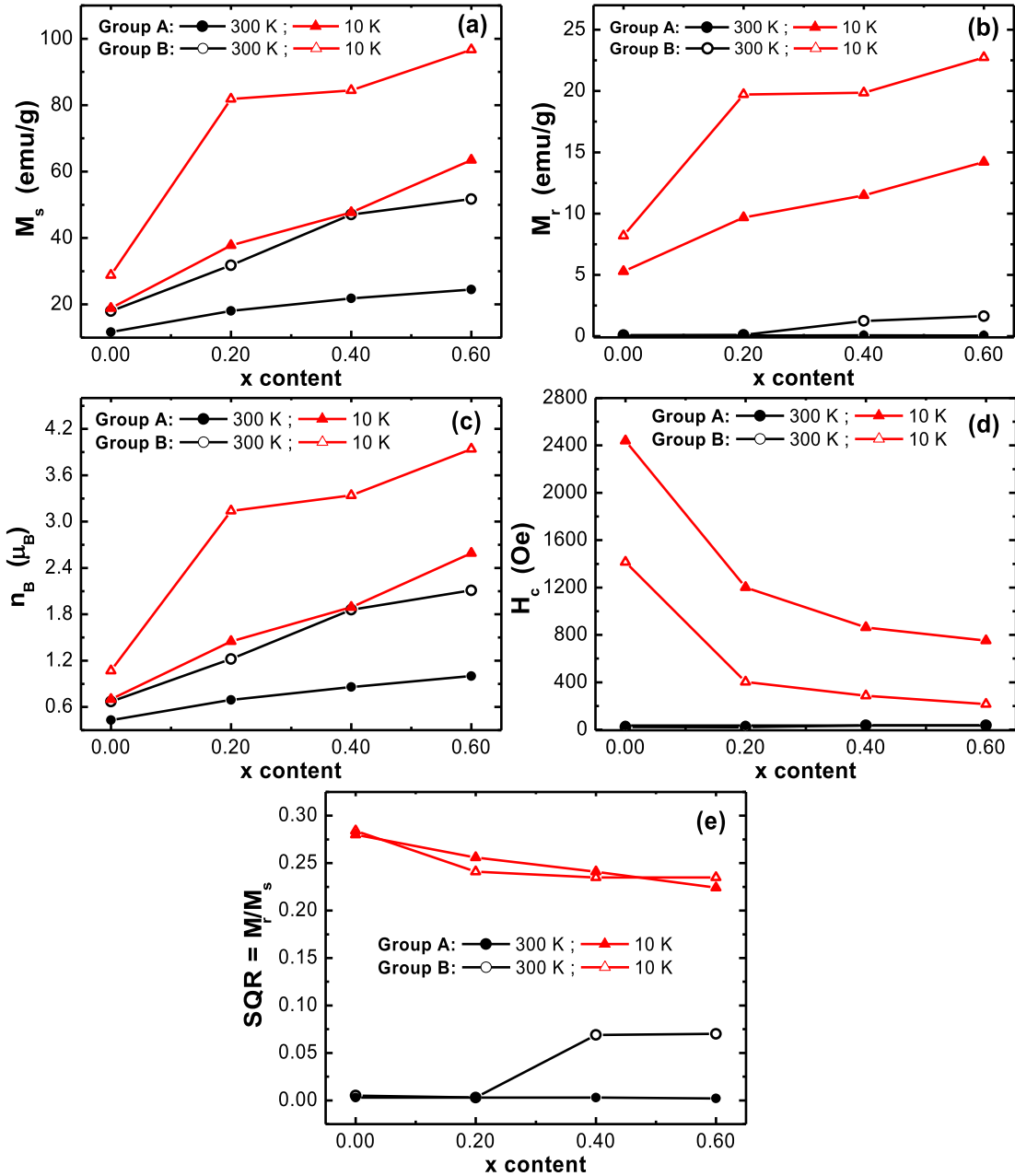


**Fig. 9** Variations of (a)  $M_s$ , (b)  $M_r$ , (c)  $n_B$ , (d)  $H_c$ , and (e) SQR with respect to Zn doping content for  $Zn_xCa_{0.5-x/2}Mg_{0.5-x/2}Fe_2O_4$  NSFs for groups A and B.

negligible, which is ascribed to the improvement in A-B interactions. Upon  $Zn^{2+}$  doping into CaMg spinel ferrite, the  $Zn^{2+}$  ions will tend to reside in the  $T_d$  sites. This will also push the  $Fe^{3+}$  ions that display large magnetic moment ( $5 \mu_B$ ) to transfer from the  $T_d$  sites towards the  $O_h$  site, which lead to rising  $Fe^{3+}$  ions at  $O_h$  sites and reducing  $Fe^{3+}$  ions at  $T_d$  sites. Consequently, the net magnetic moment in  $T_d$  sites is reduced, whereas the net moment in  $O_h$  sites is enhanced. As stated above, the resulting magnetic moment of the spinel ferrite is the difference in magnetic moments of  $T_d$  and  $O_h$  lattices. Hence, the net magnetization is further increased due to the improvement of A-B interactions with Zn substitution into CaMg NSFs.

The magneton number ( $n_B$ ) per formula unit in  $\mu_B$  was calculated for all samples using the following relation (Almessiere et al., 2019; Almessiere et al., 2019):

$$n_B = (\text{molweight} \times M_s)/5585 \quad (6)$$

The obtained  $n_B$  values are presented with respect to  $Zn^{2+}$  doping content in Fig. 9(c). It is clear that the  $n_B$  values at both temperatures and for all samples increase with the rise in the content of  $Zn^{2+}$  ions within the CaMg ferrite lattice. The findings were displayed analogous trend of  $M_s$  values versus  $Zn^{2+}$  content. This is in line with the variations in the  $M_s$  values. The increase in  $n_B$  value upon  $Zn^{2+}$  ions doping is correlated to the increase in A-B super-exchange interactions.

Another plausible reason for the increase of  $M_s$  values upon Zn doping into CaMg NSFs could be correlated to the variations in crystallites size and/or particles size. Usually,  $M_s$  value increase or decrease with the enlargement or reduction in crystallites size and/or particles size, respectively. In the present study, the structural and morphological analyses showed an increase in the crystallites size and particles size with the rise in the  $Zn^{2+}$  ions content, and hence the  $M_s$  value would increase.

At lower temperatures, the different prepared samples showed opened M–H hysteresis loops. It is observed that the coercivity is large in samples prepared without using *Moringa oleifera* extract (Group B samples) compared to those prepared using *Moringa oleifera* extract (Group A samples). It is well-known that the coercive field ( $H_c$ ) and particles size are inversely proportional (Adeela et al., 2018). In the present study, it is found that samples prepared using *Moringa oleifera* extract (Group A samples) displayed smaller particles size than those in products prepared without using *moringa oleifera* extract (Group B samples). Consequently, samples prepared using *Moringa oleifera* extract (Group A samples) would display larger coercivity than for samples prepared without using *Moringa oleifera* extract (Group B samples). At lower temperature, the  $H_c$  values for both  $Zn_xCa_{0.5-x/2}Mg_{0.5-x/2}Fe_2O_4$  ( $x = 0.0\text{--}0.6$ ) NSFs of both groups A and B decrease with increasing the doping content of  $Zn^{2+}$  ions. This indicates a decrease in the ferromagnetic behavior at 10 K with the rise in  $Zn^{2+}$  content. Generally, it is well recognized that the coercive field is varying inversely with the grains size (Almessiere et al., 2019). It is obvious that the magnetization in magnetic spinel ferrites acquired via the domain walls motion and domain rotations, and the coercive force is attained by reversing the directions of the walls motion and that of the domain rotations. The products having larger grains size would display higher number of domain walls. As the number of domain walls increases, the movement of domain walls will increase during the magnetization or demagnetization process. The motion of domain walls necessitates an energy lesser than that required by the rotation of domains. Consequently, the product exhibiting larger size of grains is anticipated to illustrate lower value of coercivity. Contrariwise, tinier nanoparticles comprise of smaller amount of domain walls, and hence need greater force for the demagnetization (Verma and Dube, 2005). Such finding is consistent with the structural and morphological investigations.

#### 4. Conclusion

The Zn substituted Mg-Ca nano-spinel ferrite as  $Zn_xCa_{0.5-x/2}Mg_{0.5-x/2}Fe_2O_4$  ( $x = 0.0\text{--}0.6$ ) NSFs, were produced efficaciously by biosynthesis *Moringa oleifera* leaf extraction linked with Ultrasound irradiation and with Ultrasound irradiation only. The XRD pattern approved the good agreement between the structure of NSFs and the standard cubic spinel ferrite. The SEM and TEM showed the difference in morphology among both groups (group A and B). The analyses of magnetization measurements revealed the SPM behavior at room temperature (300 K) for NSFs of both groups A and B. At room temperature, all prepared nanoparticles display SQR values lower than 0.1, which confirm their SPM behavior. At lower temperature ( $T = 10$ ), a transition from SPM to FM behavior has occurred. SQR values at 10 K for

NSFs of both group A and B are between 0.2 and 0.3, which is below the theoretical limit of 0.5, reflecting the NPs consist of multi-magnetic domains. The prepared samples using *Moringa oleifera* extract (Group A samples) displayed lower  $M_s$  values than those prepared without using *Moringa oleifera* extract (Group B samples). However,  $H_c$  values are found to be wider for Group B samples than Group A samples. These is mainly ascribed to the variations in particles size upon the use of *Moringa oleifera* extract. It is showed that the  $M_s$  and  $n_B$  values increase upon the doping and increase of  $Zn^{2+}$  ions content at room and low temperatures. This could be explained based on the distribution of different cations between Td and Oh sites, changes in magnetic moments, variations in crystallites or particles size, strength of the exchange interactions, etc. The  $H_c$  values were found to decrease at 10 K with rise of the  $Zn^{2+}$  content, which is attributed to the larger crystallites/particles that lead to lower volume fraction of grains boundaries, which in turn conduce to less pinning of domain walls. According to the obtained results, one can consider the use of *Moringa oleifera*-extracted solution as an alternative green synthesis route with effective and well control of structural, morphological, and physical properties of ferrite nanoparticles.

#### Declaration of Competing Interest

The authors declare that they have no known competing financial interests or personal relationships that could have appeared to influence the work reported in this paper.

#### Acknowledgment

The authors are thankful to the Institute for Research and Medical Consultations (IMRC) of Imam Abdulrahman Bin Faisal University (IAU – Saudi Arabia) for providing lab facilities.

#### References

- Abraham, A.R., Raneesh, B., Joseph, S., Mohammed Arif, P., Nambisan, P.M.G., Das, D., Rouxel, D., Oluwafemi, O.S., Thomas, S., Kalarikkal, N., 2019. Magnetic performance and defect characterization studies of core-shell architected  $MgFe_2O_4@BaTiO_3$  multiferroic nanostructures. *Phys. Chem. Chem. Phys.* 21, 8709–8720.
- Adeela, N., Khan, U., Naz, S., Khan, K., Sagar, R.U.R., Aslam, S., Wu, D., 2018. Role of Ni concentration on structural and magnetic properties of inverse spinel Ferrite. *Mater. Res. Bull.* 107, 60–65.
- Ahmad, S.I., Ansari, S.A., Kumar, D.R., 2018. Structural, morphological, magnetic properties and cation distribution of Ce and Sm co-substituted nano crystalline cobalt ferrite. *Mater. Chem. Phys.* 208, 248–257.
- Asida, S.O., Madubuonu, N., Alnasir, M.H., Ahmad, I., Botha, S., Maaza, M., Ezema, F.I., 2020. Biogenic synthesis of iron oxide nanorods using *Moringa oleifera* leaf extract for antibacterial applications. *Appl. Nanosci.* 10, 305–315.
- Akhtar, M.S., Panwar, J., Yun, Y.-Sang, 2013. Biogenic synthesis of metallic nanoparticles by plant extracts. *ACS Sustain. Chem. Eng.* 1, 591–602.
- Akhtar, S., Rehman, S., Almessiere, M.A., Khan, F.A., Slimani, Y., Baykal, A., 2019. Synthesis of  $Mn_{0.5}Zn_{0.5}Sm_xEu_xFe_{1.8-2x}O_4$  nanoparticles via the hydrothermal approach induced anti-cancer and anti-bacterial activities. *Nanomaterials*. 9, 1635.

- Almessiere, M.A.A., Slimani, Y., Sertkol, M., Khan, F.A.A., Nawaz, M., Tombuloglu, H., Al-Suhaimi, E.A.A., Baykal, A., 2019. Ce-Nd Co-substituted nanospinel cobalt ferrites: An investigation of their structural, magnetic, optical, and apoptotic properties. *Ceram. Int.* 45, 16147–16156.
- Almessiere, M.A., Slimani, Y., Güner, S., Nawaz, M., Baykal, A., Aldakheel, F., Akhtar, S., Ercan, I., Belenli, B. Ozçelik, 2019. Magnetic and structural characterization of Nb<sup>3+</sup>-substituted CoFe<sub>2</sub>O<sub>4</sub> nanoparticles. *Ceram. Int.* 45, 8222–8232.
- Almessiere, M.A., Slimani, Y., Sertkol, M., Nawaz, M., Baykal, A., Ercan, I., 2019. The impact of Zr substituted Sr hexaferrite: Investigation on structure, optic and magnetic properties. *Results Phys.* 13, 102244.
- Almessiere, M.A., Slimani, Y., Rehman, S., Khan, F.A., Güngüneş, D., Güner, S., Shirsath, S.E., Baykal, A., 2020. Magnetic properties, anticancer and antibacterial effectiveness of sonochemically produced Ce<sup>3+</sup>/Dy<sup>3+</sup> co-activated Mn-Zn nanospinel ferrites. *Arab. J. Chem.* 13, 7403–7417.
- Almessiere, M., Slimani, Y., Korkmaz, A.D., Güner, S., Baykal, A., Shirsath, S., Ercan, I., Kögerler, P., 2020. Sonochemical synthesis of Dy<sup>3+</sup> substituted Mn<sub>0.5</sub>Zn<sub>0.5</sub>Fe<sub>2-x</sub>O<sub>4</sub> nanoparticles: Structural, magnetic and optical characterizations. *Ultrason Sonochem* 61, 104836.
- Almessiere, M.A., Trukhanov, A.V., Khan, F.A., Slimani, Y., Tashkandi, N., Turchenko, V.A., Zubari, T.I., Tishkevich, D.I., Trukhanov, S.V., Panina, L.V., Baykal, A., 2020. Correlation between microstructure parameters and anti-cancer activity of the [Mn<sub>0.5</sub>Zn<sub>0.5</sub>](Eu<sub>x</sub>Nd<sub>x</sub>Fe<sub>2-2x</sub>)O<sub>4</sub> nanoferrites produced by modified sol-gel and ultrasonic methods. *Ceram. Int.* 46, 7346–7354.
- Alves, C., Aquino, R., Depeyrot, J., Cotta, T.P., Sousa, M., Tourinho, F., Rechenberg, H., Goya, G., 2006. Surface spin freezing of ferrite nanoparticles evidenced by magnetization measurements. *J. Appl. Phys.* 99, 08M905.
- Amiri, M., Salavati-Niasari, M., Akbari, A., 2019. Magnetic nanocarriers: evolution of spinel ferrites for medical applications. *Adv. Colloid Interface Sci.* 265, 29–44.
- Anastas, P., Eghbali, N., 2010. Green chemistry: principles and practice. *Chem. Soc. Rev.* 39, 301–312.
- Asiri, S., Sertkol, M., Guner, S., Gungunes, H., Batoo, K., Saleh, T. A., Sozeri, H., Almessiere, M.A., Manikandan, A., Baykal, A., 2018. Hydrothermal synthesis of Co<sub>y</sub>Zn<sub>1-y</sub>Mn<sub>1-2y</sub>Fe<sub>2</sub>O<sub>4</sub> nanoferrites: magneto-optical investigation. *Ceram. Int.* 44, 5751–5759.
- Bektar, M., Rasekh, H.A., Soltanianfard, M.J., 2020. Synthesis and characterization of CoFe<sub>2</sub>O<sub>4</sub>@SiO<sub>2</sub>-polyethyleneimine magnetic nanoparticle and its application for ultrasonic-assisted removal of disulfine blue dye from aqueous solution. *Arab. J. Chem.* 13, 5430–5437.
- Cardoso, B.D., Rio, I.S.R., Rodrigues, A.R.O., Fernandes, F.C.T., Almeida, B.G., Pires, A., Pereira, A.M., Araújo, J.P., Castanheira, E.M.S., Coutinho, P.J.G., 2018. Magnetoliposomes containing magnesium ferrite nanoparticles as nanocarriers for the model drug curcumin. *R. Soc. Open Sci.* 5.
- Chavarriaga, E., Lopera, A., Franco, V., Bergmann, C., Alarcón, J., 2020. Gel combustion synthesis and magnetic properties of CoFe<sub>2</sub>O<sub>4</sub>, ZnFe<sub>2</sub>O<sub>4</sub>, and MgFe<sub>2</sub>O<sub>4</sub> using 6-aminohexanoic acid as a new fuel. *J. Magn. Magn. Mater.* 497, 166054.
- B.D. Cullity, Introduction to Magnetic Materials, Addison-Wesley, Reading, MA, 1972, 141.
- Dora, B.B., Kumar, S., Sahu, M., Mast, B., 2014. Size controlled synthesis and magnetic behaviour of Mg-Zn nano ferrites by using Aloe vera extract solution. *Int. J. Pharm. Sci. Rev. Res.* 29, 307–311.
- dos Santos, J.M., Pereira, C.R., Foletto, E.L., Dotto, G.L., 2019. Alternative synthesis for ZnFe<sub>2</sub>O<sub>4</sub>/chitosan magnetic particles to remove diclofenac from water by adsorption. *Int. J. Biol. Macromol.* 131, 301–308.
- Elayakumar, K., Manikandan, A., Dinesh, A., Thanrasu, K., Kanmani Raja, K., Thilak Kumar, R., Slimani, Y., Jaganathan, S.K., Baykal, 2019. Enhanced magnetic property and antibacterial biomedical activity of Ce<sup>3+</sup> doped CuFe<sub>2</sub>O<sub>4</sub> spinel nanoparticles synthesized by sol-gel method. *J. Magn. Magn. Mater.* 478, 140–147.
- Fella, O.O., Tamine, M., Randrianantoandro, N., Grenèche, J., 2013. Microstructural studies of milled and annealed ZnFe<sub>2</sub>O<sub>4</sub> nanostructures using X-ray diffraction and Mössbauer Spectroscopy. *Nanosci. Nanotechnol.* 1, 1–6.
- Gunasekaran, S., Thanrasu, K., Manikandan, A., Durka, M., Dinesh, A., Anand, S., Shankar, S., Slimani, Y., Almessiere, M.A., Baykal, A., 2021. Structural, fabrication and enhanced electromagnetic wave absorption properties of reduced graphene oxide (rGO)/zirconium substituted cobalt ferrite (Co<sub>0.5</sub>Zr<sub>0.5</sub>Fe<sub>2</sub>O<sub>4</sub>) nanocomposites. *Phys. B* 605, 412784.
- Huang, Y., Tang, Y., Wang, J., Chen, Q., 2006. Synthesis of MgFe<sub>2</sub>O<sub>4</sub> nanocrystallites under mild conditions. *Mater. Chem. Phys.* 97, 394–397.
- Hussain, M., Meydan, T., Cuenda, J.A., Melikhov, Y., Mustafa, G., Murtaza, G., Jamil, Y., 2018. Microwave absorption properties of CoGd substituted ZnFe<sub>2</sub>O<sub>4</sub> ferrites synthesized by co-precipitation technique. *Ceram. Int.* 44, 5909–5914.
- Jiang, B., Han, C., Li, B., He, Y., Lin, Z., 2016. In-situ crafting of ZnFe<sub>2</sub>O<sub>4</sub> nanoparticles impregnated within continuous carbon network as advanced anode materials. *Acs Nano* 10, 2728–2735.
- Kgatitsoe, M.M., 2018. Synthesis of magnetic sorbents modified with *Moringa oleifera* extracts for the removal of environmental organic pollutants Master Thesis. University of the Witwatersrand, Johannesburg.
- Kondo, T., Kurokawa, A., Takeuchi, H., Yanoh, T., Yano, S., Onuma, K., Miike, K., Miyasaka, T., Ichiyangai, Y., 2013. Magnetic properties of MgFe<sub>2</sub>O<sub>4</sub> nanoparticles and Zn doping effect. *Trans. Mater. Res. Soc. Japan.* 38, 513–516.
- Lal, G., Punia, K., Dolia, S.N., Alvi, P.A., Dalela, S., Kumar, S., 2019. Rietveld refinement, Raman, optical, dielectric, Mössbauer and magnetic characterization of superparamagnetic fcc-CaFe<sub>2</sub>O<sub>4</sub> nanoparticles. *Ceram. Int.* 45, 5837–5847.
- Li, F., Wang, H., Wang, L., Wang, J., 2007. Magnetic properties of ZnFe<sub>2</sub>O<sub>4</sub> nanoparticles produced by a low-temperature solid-state reaction method. *J. Magn. Magn. Mater.* 309, 295–299.
- Liang, P.-L., Yuan, L.-Y., Deng, H., Wang, X.-C., Wang, L., Li, Z.-J., Luo, S.-Z., Shi, W.-Q., 2020. Photocatalytic reduction of uranium (VI) by magnetic ZnFe<sub>2</sub>O<sub>4</sub> under visible light. *Appl. Catal. B.* 267, 118688.
- Madubuonu, N., Aisida, S.O., Ali, A., Ahmad, I., Zhao, T., Botha, S., Maaza, M., Ezema, F.I., 2019. Biosynthesis of iron oxide nanoparticles via a composite of *Psidium guajava*-*Moringa oleifera* and their antibacterial and photocatalytic study. *J. Photochem. Photobiol. B: Biol.* 199, 111601.
- Manikandan, A., Judith Vijaya, J., Sundararajan, M., Meganathan, C., Kennedy, L.J., Bououdina, M., 2013. Optical and magnetic properties of Mg-doped ZnFe<sub>2</sub>O<sub>4</sub> nanoparticles prepared by rapid microwave combustion method. *Superlattices Microstruct.* 64, 118–131.
- Mapossa, Antonio B., Dantas, J., Silva, M.R., Kiminami, Ruth H.G. A., Costa, Ana Cristina F.M., Daramola, Michael O., 2020. Catalytic performance of NiFe<sub>2</sub>O<sub>4</sub> and Ni<sub>0.3</sub>Zn<sub>0.7</sub>Fe<sub>2</sub>O<sub>4</sub> magnetic nanoparticles during biodiesel production. *Arab. J. Chem.* 13, 4462–4476.
- Martinez-Julian, F., Guerrero, A., Haro, M., Bisquert, J., Bresser, D., Paillard, E., Passerini, S., Garcia-Belmonte, G., 2014. Probing lithiation kinetics of carbon-coated ZnFe<sub>2</sub>O<sub>4</sub> nanoparticle battery anodes. *J. Phys. Chem* 118, 6069–6076.
- Matinise, N., Kaviyarasu, K., Mongwaketsi, N., Khamlich, S., Kotsedi, L., Mayedwa, N., Maaza, M., 2018. Green synthesis of novel zinc iron oxide (ZnFe<sub>2</sub>O<sub>4</sub>) nanocomposite via Moringa Oleifera natural extract for electrochemical applications. *Appl. Surf. Sci.* 446, 66–73.

- Mozaffari, M., Eghbali Arani, M., Amighian, J., 2010. The effect of cation distribution on magnetization of  $ZnFe_2O_4$  nanoparticles. *J. Magn. Magn. Mater.* 322, 3240–3244.
- Murugesan, C., Chandrasekaran, G.J.R.A., 2015. Impact of  $Gd^{3+}$  substitution on the structural, magnetic and electrical properties of cobalt ferrite nanoparticles. *RSC Adv.* 5, 73714–73725.
- Ndabigengesere, A., Narasiah, K.S., Talbot, B.G., 1995. Active agents and mechanism of coagulation of turbid waters using *Moringa oleifera*. *Water Res.* 29, 703.
- Pastucha, M., Farka, Z., Lacina, K., Mikušová, Z., Skládal, P., 2019. Magnetic nanoparticles for smart electrochemical immunoassays: a review on recent developments. *Microchim. Acta* 186, 312.
- Pereira, D.S., Cardoso, B.D., Rodrigues, A.R.O., Amorim, C.O., Amaral, V.S., Almeida, B.G., Queiroz, M.J.R., Martinho, O., Baltazar, F., Calhelha, R.C. and Ferreira, I.C., 2019. Magnetoliposomes containing calcium ferrite nanoparticles for applications in breast cancer therapy. *Pharmaceutics* 11, 477.
- Phumying, S., Labuayai, S., Swatsitang, E., Amornkitbamrung, V., Maensiri, S., 2013. Nanocrystalline spinel ferrite ( $MFe_2O_4$ ,  $M = Ni, Co, Mn, Mg, Zn$ ) powders prepared by a simple aloe vera plant-extracted solution hydrothermal route. *Mater. Res. Bull.* 48, 2060–2065.
- Prasad, C., Sreenivasulu, K., Gangadhara, S., Venkateswarlu, P., 2017. Bio inspired green synthesis of  $Ni/Fe_3O_4$  magnetic nanoparticles using *Moringa oleifera* leaves extract: A magnetically recoverable catalyst for organic dye degradation in aqueous solution. *J. Alloys Compd.* 700, 252–258.
- Rahman, S., Nadeem, K., Anis-Ur-Rehman, M., Mumtaz, M., Naeem, S., Letofsky-Papst, I., 2013. Structural and magnetic properties of  $ZnMg$ -ferrite nanoparticles prepared using the co-precipitation method. *Ceram. Int.* 39, 5235–5239.
- Rahmayeni, Alfina, A., Stiadi, Y., Lee, H.J., Zulhadjri, 2019. Green synthesis and characterization of  $ZnO$ - $CoFe_2O_4$  semiconductor photocatalysts prepared using Rambutan (*Nephelium lappaceum* L.) Peel Extract, *Mater. Res.* 22 (2019).
- Ramarao, K., Rajesh Babu, B., Kishore Babu, B., Veeraiah, V., Ramarao, S.D., Rajasekhar, K., Venkateswara Rao, A., 2018. Influence of Zn Substitution on Structural, Magnetic and Electrical Properties of  $MgFe_2O_4$ . *J. Electron. Mater.* 47, 2997–3004.
- Rashad, M.M., 2007. Magnetic properties of nanocrystalline magnesium ferrite by co-precipitation assisted with ultrasound irradiation. *J. Mater. Sci.* 42, 5248–5255.
- Rivero, M., del Campo, A., Mayoral, Á., Mazario, E., Sánchez-Marcos, J., Muñoz-Bonilla, A., 2016. Synthesis and structural characterization of  $Zn_xFe_{3-x}O_4$  ferrite nanoparticles obtained by an electrochemical method. *RSC Adv.* 6, 40067–40076.
- Sathyavathi, R., Krishna, M., Rao, D.N., 2011 Mar 1. Biosynthesis of silver nanoparticles using *Moringa oleifera* leaf extract and its application to optical limiting. *J. Nanosci. Nanotechnol.* 11 (3), 2031–2035.
- Sharma, R., Yadav, S., Gupta, R., Arora, G., 2019. Synthesis of magnetic nanoparticles using potato extract for dye degradation: A green chemistry experiment. *J. Chem. Educ.* 96, 3038–3044.
- Shirsath, S.E., Wang, D., Jadhav, S.S., Mane, M.L., Li, S., 2018. Ferrites obtained by sol-gel method. In: Klein, L., Aparicio, M., Jitianu, A. (Eds.), *Handbook of Sol-Gel Science and Technology*, Springer, Cham, 2018, pp. 695–735.
- Shirsath, S.E., Mane, M.L., Yasukawa, Y., Liu, X., Morisako, A., 2013. Chemical tuning of structure formation and combustion process in  $CoDy_{0.1}Fe_{1.9}O_4$  nanoparticles: influence@pH. *J. Nanopart. Res.* 15, 1976.
- Shirsath, S.E., Mane, M.L., Yasukawa, Y., Liu, X., Morisako, A., 2014. Self-ignited high temperature synthesis and enhanced super-exchange interactions of  $Ho^{3+}$ – $Mn^{2+}$ – $Fe^{3+}$ – $O^{2-}$  ferromagnetic nanoparticles. *Phys. Chem. Chem. Phys.* 16, 2347–2357.
- Slimani, Y., Almessiere, M.A., Nawaz, M., Baykal, A., Akhtar, S., Ercan, I., Belenli, I., 2019. Effect of bimetallic (Ca, Mg) substitu- tion on magneto-optical properties of  $NiFe_2O_4$  nanoparticles. *Ceram. Int.* 45, 6021–6029.
- Slimani, Y., Almessiere, M.A., Sertkol, M., Shirsath, S.E., Baykal, A., Nawaz, M., Akhtar, S., Ozcelik, B., Ercan, I., 2019. Structural, magnetic, optical properties and cation distribution of nanosized  $Ni_{0.3}Cu_{0.3}Zn_{0.4}Tm_xFe_{2-x}O_4$  ( $0.0 \leq x \leq 0.10$ ) spinel ferrites synthesized by ultrasound irradiation. *Ultrason. Sonochem.* 57, 203–211.
- Slimani, Y., Almessiere, M.A., Demir Korkmaz, A., Guner, S., Güngüneş, H., Sertkol, M., Manikandan, A., Yıldız, A., Akhtar, S., Shirsath, Sagar E., Baykal, A., 2019.  $Ni_{0.4}Cu_{0.2}Zn_{0.4}Tb_xFe_{2-x}O_4$  nanospinel ferrites: ultrasonic synthesis and physical properties. *Ultrason. Sonochem.* 59, 104757.
- Smaranika, D., Umesh, K.P., Birendra, K.B., 2013. Green biosynthesis of Silver nano particles using *Moringa oleifera* leaf. *Inter. J. Nanotech. Appl. (IJNA)* 3 (2), 51–62.
- Srivastava, M., Alla, S., Meena, S.S., Gupta, N., Mandal, R., Prasad, N., 2018.  $Zn_xFe_{3-x}O_4$  ( $0.01 \leq x \leq 0.8$ ) nanoparticles for controlled magnetic hyperthermia application. *New J. Chem.* 42, 7144–7153.
- Sulaiman, N.H., Ghazali, M.J., Yunas, J., Rajabi, A., Majlis, B.Y., Razali, M., 2018. Synthesis and characterization of  $CaFe_2O_4$  nanoparticles via co-precipitation and auto-combustion methods. *Ceram. Int.* 44, 46–50.
- Sutherland, J.P., Folkard, G.K., Mtawali, M.A., Grant, W.D., 1994. 20th WEDC Conference Colombo, Sri Lanka, August (1994), p. 297.
- Thummer, K.P., Chhantbar, M.C., Modi, K.B., Baldha, G.J., Joshi, H.H., 2004. Localized canted spin behaviour in  $Zn_xMg_{1.5-x}Mn_{0.5-x}FeO_4$  spinel ferrite system. *J. Magn. Magn. Mater.* 280, 23–30.
- Tovar, G.I., Briceño, S., Suarez, J., Flores, S., González, G., 2020. Biogenic synthesis of iron oxide nanoparticles using *Moringa oleifera* and chitosan and its evaluation on corn germination. *Environ. Nanotechnol. Monit. Manag.* 14, 100350.
- Venkateswarlu, S., Kumar, B.N., Prathima, B., Anitha, K., Jyothi, N., 2015. A novel green synthesis of  $Fe_3O_4$ -Ag core shell recyclable nanoparticles using *Vitis vinifera* stem extract and its enhanced antibacterial performance. *Phys. Rev. B Condens. Matter.* 457, 30–35.
- Vergaro, V., Scarlino, F., Bellomo, C., Rinaldi, R., Vergara, D., Maffia, M., Baldassarre, F., Giannelli, G., Zhang, X., Lvov, Y.M., 2011. Drug-loaded polyelectrolyte microcapsules for sustained targeting of cancer cells. *Adv. Drug Deliv. Rev.* 63, 847–864.
- Verma, A., Dube, D.C., 2005. Processing of nickel-zinc ferrites via the citrate precursor route for high-frequency applications. *J. Am. Ceram. Soc.* 88, 519–523.
- Vinosa, P.A.A., Manikandan, A., Ragu, R., Dinesh, A., Thanrasu, K., Slimani, Y., Baykal, A., Xavier, B., 2020. Impact of nickel substitution on structure, magneto-optical, electrical and acoustical properties of cobalt ferrite nanoparticles. *J. Alloys Compd.* 157517.
- Vinosa, P.A.A., Manikandan, A., Ragu, R., Dinesh, A., Paulraj, P., Slimani, Y., Almessiere, M.A., Baykal, A., Madhavan, J., Xavier, B., Nirmala, G.F., 2020. Exploring the influence of varying pH on structural, electro-optical, magnetic and photo-Fenton properties of mesoporous  $ZnFe_2O_4$  nanocrystals. *Environ. Pollut.* 115983.
- Waldron, R., 1955. Infrared spectra of ferrites. *Phys. Rev.* 99, 1727.
- Wang, S., Li, D., Yang, C., Sun, G., Zhang, J., Xia, Y., Xie, C., Yang, G., Zhou, M., Liu, W., 2017. A novel method for the synthesize of nanostructured  $MgFe_2O_4$  photocatalysts. *J. Sol-Gel Sci. Technol.* 84, 169–179.
- Won, J.M., Choi, S.H., Hong, Y.J., Ko, Y.N., Kang, Y.C., 2014. Electrochemical properties of yolk-shell structured  $ZnFe_2O_4$  powders prepared by a simple spray drying process as anode material for lithium-ion battery. *Sci. Rep.* 4, 5857.
- Xing, Z., Ju, Z., Yang, J., Xu, H., Qian, Y., 2012. One-step hydrothermal synthesis of  $ZnFe_2O_4$  nano-octahedrons as a high capacity anode material for Li-ion batteries. *Nano Res.* 5, 477–485.
- Yao, C., Zeng, Q., Goya, G., Torres, T., Liu, J., Wu, H., Ge, M., Zeng, Y., Wang, Y., Jiang, J., 2007.  $ZnFe_2O_4$  nanocrystals: synthesis and magnetic properties. *J. Phys. Chem. C.* 111, 12274–12278.

- Yunas, J., Sulaiman, N.H., Ghazali, M.J., 2018. Comparative study of the calcium ferrite nanoparticles (CaFe<sub>2</sub>O<sub>4</sub>-NPs) synthesis process. In: IEEE Int. Conf. Semicond. Electron. Proceedings, ICSE, Institute of Electrical and Electronics Engineers Inc., pp. 101–103.
- Zhang, M., Liu, Y., Zhu, H., Wang, X., 2020. Hierarchical bead chain ZnFe<sub>2</sub>O<sub>4</sub>-PEDOT composites with enhanced Li-ion storage properties as anode materials for lithium-ion batteries. *Appl. Surf. Sci.* **529**, 147078.
- Zhou, X., Li, X., Sun, H., Sun, P., Liang, X., Liu, F., Hu, X., Lu, G., 2015. Nanosheet-assembled ZnFe<sub>2</sub>O<sub>4</sub> hollow microspheres for high-sensitive acetone sensor. *ACS Appl. Mater. Interfaces* **7**, 15414–15421.